


Article

RuCo Alloy Nanoparticles Embedded into N-Doped Carbon for High Efficiency Hydrogen Evolution Electrocatalyst

Cheng Wang^{1,2}, Yibo Wang², Zhaoping Shi², Wenhua Luo^{1,3}, Junjie Ge², Wei Xing^{2,*}, Ge Sang^{1,3,*} and Changpeng Liu^{2,*} 

¹ Science and Technology on Surface Physics and Chemistry Laboratory, Jiangyou 621908, China; wangcheng@ciac.ac.cn (C.W.); luowenhua@caep.cn (W.L.)

² State Key Laboratory of Electroanalytical Chemistry, Laboratory of Advanced Power Sources, Changchun Institute of Applied Chemistry, Chinese Academy of Sciences, Changchun 130022, China; bowang@ciac.ac.cn (Y.W.); zpshi@ciac.ac.cn (Z.S.); gejj@ciac.ac.cn (J.G.)

³ Institute of Materials, China Academy of Engineering Physics, Jiangyou 621907, China

* Correspondence: xingwei@ciac.ac.cn (W.X.); angelsg@163.com (G.S.); liuchp@ciac.ac.cn (C.L.)

Abstract: For large-scale and sustainable water electrolysis, it is of great significance to develop cheap and efficient electrocatalysts that can replace platinum. Currently, it is difficult for most catalysts to combine high activity and stability. To solve this problem, we use cobalt to regulate the electronic structure of ruthenium to achieve high activity, and use carbon matrix to protect alloy nanoparticles to achieve high stability. Herein, based on the zeolitic imidazolate frameworks (ZIFs), a novel hybrid composed of RuCo alloy nano-particles and N-doped carbon was prepared via a facile pyrolysis-displacement-sintering strategy. Due to the unique porous structure and multi-component synergy, the optimal RuCo500@NC750 material in both acidic and alkaline media exhibited eminent HER catalytic activity. Notably, the 3-RuCo500@NC750 obtained a current density of 10 mA cm⁻² at 22 mV and 31 mV in 0.5 M H₂SO₄ and 1.0 M KOH, respectively, comparable to that of the reference Pt/C catalyst. Furthermore, the Tafel slopes of the catalyst are 52 mV Dec⁻¹ and 47 mV Dec⁻¹, respectively, under acid and alkali conditions, and the catalyst has good stability, indicating that it has broad application prospects in practical electrolytic systems. This work contributes to understanding the role of carbon-supported polymetallic alloy in the electrocatalytic hydrogen evolution process, and provides some inspiration for the development of a high efficiency hydrogen evolution catalyst.

Keywords: electrocatalysis; hydrogen evolution reaction (HER); water splitting; hydrogen production; RuCo alloy



Citation: Wang, C.; Wang, Y.; Shi, Z.; Luo, W.; Ge, J.; Xing, W.; Sang, G.; Liu, C. RuCo Alloy Nanoparticles Embedded into N-Doped Carbon for High Efficiency Hydrogen Evolution Electrocatalyst. *Energies* **2022**, *15*, 2908. <https://doi.org/10.3390/en15082908>

Academic Editor: Dmitri A. Bulushev

Received: 23 March 2022

Accepted: 12 April 2022

Published: 15 April 2022

Publisher's Note: MDPI stays neutral with regard to jurisdictional claims in published maps and institutional affiliations.



Copyright: © 2022 by the authors. Licensee MDPI, Basel, Switzerland. This article is an open access article distributed under the terms and conditions of the Creative Commons Attribution (CC BY) license (<https://creativecommons.org/licenses/by/4.0/>).

1. Introduction

To address the global energy crisis and achieve carbon neutrality, it is urgent to find a clean and sustainable new energy source [1,2]. Hydrogen energy has the advantages of zero emissions, high energy density and recyclability, making it an ideal substitute for traditional fossil fuels [3]. So far, the most environmentally friendly and sustainable method to produce high purity hydrogen is water electrolysis [4,5]. However, this takes a lot of electric power to overcome the overpotential [6]. At present, platinum is the best catalyst for the hydrogen evolution reaction in industry [7], but its application is restricted by its low reserves and high cost [8,9]. Therefore, the development of efficient, cheap and abundant hydrogen evolution catalysts that can replace platinum has become the focus of research attention.

Over the past decades, although a great number of endeavors have been made to develop high performance hydrogen evolution transition element compound catalysts, such as metal sulfides and phosphides [10,11], there are still some shortcomings [12]. Generally speaking, the ideal electrocatalyst for hydrogen evolution should have moderate H adsorption strength [13,14]. Because the bonding strength of Ru-H (~65 kcal mol⁻¹) [15]

is similar to that of Pt-H ($\sim 62 \text{ kcal mol}^{-1}$) [16] and its price is well below that of other platinum group metals, ruthenium based materials have attracted extensive attention in the field of HER electrocatalysis [17]. Javeed Mahmood et al. developed an efficient and pH-universal ruthenium-based catalyst for the hydrogen evolution reaction, and its hydrogen evolution overpotential at 10 mA cm^{-2} in $0.5 \text{ M H}_2\text{SO}_4$ and 1.0 M KOH is only 13.5 mV and 17.0 mV , respectively [18]. Wei Wang et al. used ruthenium nanoparticles loaded on carbon oxide nanotubes to electrocatalyze hydrogen evolution in an alkaline medium, and only the overpotential of 13.2 mV was needed to achieve the current density of 10 mA cm^{-2} [19]. The current limitation of platinum group metals arises from the fact that although these catalysts facilitate adsorption and recombination of active hydrogen intermediates (H_{ad}), they are generally inefficient in the first step of water dissociation [20,21]. Other transition metals (e.g., Fe, Co, Ni) can effectively split the HO–H bond [22–24], but do not easily convert the generated H_{ad} intermediate into H_2 [21,25]. In addition, some studies have found that the charge distribution of the parent metal can be adjusted, and its electronic structure can be optimized by using another metal to form an alloy with it, so as to obtain appropriate metal–hydrogen binding energy and good HER performance [26–28]. Jing Dong et al. realized efficient hydrogen evolution by using mesoporous NiCo alloy/reduced graphene oxide nanocomposites, which can reach the current density of 10 mA cm^{-2} at 115 mV [29]. Hanruo Chen et al. used nanostructured PdFe alloy membranes as efficient electrocatalysts for hydrogen evolution in acidic and alkaline solutions [30]. Hence, in order to enhance the electrocatalytic activity of HER while reducing the cost, alloying a handful of Ru with another transition metal may be a viable way to achieve high HER electrocatalytic activity [27,31]. Besides high activity, boosting the stability of electrocatalysts is also important in practical applications [32]. Because of the high surface energy of metal/alloy nanoparticles (NPs), they usually encounter severe agglomeration, which leads to the degradation of catalytic activity [33]. To solve this problem, we can use the confinement effect to fix the alloy NPs into a conductive N-doped carbon matrix, which not only validly protects the alloy NPs from chemical corrosion or oxidation, inhibits the aggregation or separation of active substances, but also ensures the high conductivity of the catalyst [34–36].

ZIFs is a kind of porous crystal material formed by the interconnection of metal nodes and organic ligands [34,36]. Pyrolyzing ZIFs has become a commodious approach to prepare functional metal–carbon hybrid materials [37,38]. Therefore, we developed a simple pyrolysis-displacement-sintering strategy to directly fix RuCo alloy NPs into the nitrogen-doped carbon matrix (RuCo@NC) originating from ZIF-67 in this study. In this way, the electronic structure of Ru can be adjusted by Co to achieve high activity, and its stability can be improved by the encapsulation of the carbon matrix. Electrochemical experimental results demonstrate that the RuCo@NC has excellent electrocatalytic activity toward HER regardless of acidic or alkaline conditions, owing to the synergy between Ru and Co atoms, good conductivity, as well as abundant pores. Especially in alkaline medium it shows better performance than Pt/C, which may be attributed to Co being involved in water dissociation [39]. All in all, this material has potential applications in water electrolysis for hydrogen evolution.

2. Experimental Section

2.1. Materials

Cobalt(II) nitrate hexahydrate ($\text{Co}(\text{NO}_3)_2 \cdot 6\text{H}_2\text{O}$, Aladdin, Bay City, MI, USA, 99%) and 2-methylimidazole ($\text{C}_4\text{H}_6\text{N}_2$, Aladdin, 98%) were used to synthesize ZIF67. Methanol (CH_3OH , Xi Long Scientific, Shantou, China, 99.5%) and ethanol ($\text{C}_2\text{H}_5\text{OH}$, Xi Long Scientific, 99.5%) were used as solvent and cleaning solution, respectively. Anhydrous ruthenium(III) chloride (RuCl_3 , 3Achemical, Dhamna, India, 99%) was used to replace cobalt in carbonized ZIF67. All experiments used deionized water. The commercial Pt/C (20 wt.%) catalyst was purchased from Johnson Matthey Company.

2.2. Materials Preparation

2.2.1. Synthesis of $C_{ZIF67-T_1}$

Firstly, ZIF-67 was synthesized by a modified method similar to that reported in previous literature [40]. Typically, 3.5 g of 2-methylimidazole and 3.0 g of $Co(NO_3)_2 \cdot 6H_2O$ were dissolved in 80 mL and 40 mL of methanol under continuous agitation, respectively. The two solutions were then directly mixed, and ultrasound was performed for 10 min. Afterwards, the mixture was stirred vigorously for 24 h at room temperature. The obtained product was centrifuged with absolute alcohol four times and dried overnight at 55 °C. Secondly, the purple ZIF67 was carefully ground and placed in the quartz boat. The quartz boat was then heated to several different temperatures ($T_1 = 600, 750$ and 900 °C) at a rate of 5 °C min^{-1} in a tubular furnace under 5% H_2/Ar atmosphere and cooled naturally to indoor temperature after 2 h. The resulting black powder was collected after washing with water and labelled as $C_{ZIF67-T_1}$ (T_1 means pyrolysis temperature).

2.2.2. Synthesis of $RuCo-T_2@NC-T_1$

Firstly, 100 mg of $C_{ZIF67-T_1}$ was added to 10 mL of water in a brown reagent bottle. After ultrasonic dispersion for 30 min, a certain amount of $RuCl_3$ (as shown in Table S1) was added to the bottle and stirred vigorously for 36 h at ambient temperature. After finishing, black solids were filtered and then dried for 10 h in a vacuum. Secondly, these black solids were heated to a certain temperature ($T_2 = 300, 500$ and 700 °C) for 2 h at a rate of 5 °C min^{-1} under a 5% H_2/Ar atmosphere in a tubular furnace, and then naturally cooled to ambient temperature. Finally, the residual substance was collected and named $RuCo-T_2@NC-T_1$ (T_2 means sintering temperature).

2.2.3. Synthesis of Ru NPs/ $C_{ZIF67-750}$

Ru NPs/ $C_{ZIF67-750}$ was prepared by sodium borohydride reduction method. In order to synthesize Ru NPs/ $C_{ZIF67-750}$ catalyst with 10% Ru content, 100 mg of $C_{ZIF67-750}$ was ultrasonically dispersed in 10 mL of deionized water, and the calculated amount of $RuCl_3$ was added under intense agitation. After that, the mixed system was put into an ice bath and an excess amount of fresh $NaBH_4$ (0.5 M) aqueous solution was added dropwise. The mixture was continuously stirred for another 3 h to ensure a full reduction of Ru^{3+} . Finally, the prepared catalysts were centrifuged with water and ethanol and dried at 55 °C for 10 h.

3. Results and Discussion

3.1. Design and Characterizations of Catalysts

The detailed fabrication process of $RuCo@NC$ is clearly shown in Figure 1. Firstly, ZIF67 was synthesized by self-assembly of Co^{2+} and 2-methylimidazole. Subsequently, Ru^{3+} ions were replaced with carbonized ZIF-67 to cover the surface of Co NPs, then sintered to form $RuCo$ alloy NPs loaded on N-doped carbon. These catalysts were called 1- $RuCo-T_2@NC-T_1$, 2- $RuCo-T_2@NC-T_1$, 3- $RuCo-T_2@NC-T_1$, respectively, according to different Ru content. In addition, Ru NPs/ $C_{ZIF67-750}$ have also been synthesized by $NaBH_4$ reduction for comparison.

The structures and morphologies of all the samples obtained by SEM and TEM are displayed in Figure 2 and Figure S1. As shown in Figure 2d and Figure S1a,d, the original ZIF67 presents a three-dimensional ordered dodecahedron structure and smooth surface. Then, the prepared ZIF67 precursors were pyrolyzed in flowing H_2/Ar at different annealing temperatures. As can be seen from the SEM image (Figure S1b), the dodecahedron structure of $C_{ZIF67-750}$ is well maintained, but the particle size decreases. In the SAED pattern (Figure 2b), there are three obvious polycrystalline diffraction rings, which correspond to the (220), (200) and (111) faces of the face-centered cubic phase of Co , respectively, indicating the formation of Co nanoparticles in $C_{ZIF67-750}$. As shown in Figure 2e–g, Co NPs are uniformly dispersed in the carbon matrix, and the size of Co NPs enlarges with the increase in pyrolysis temperature. After deposition of Ru ions on the surface of carbonized ZIF67, it was sintered at different temperatures. As can be seen from

Figure S1c and Figure 2a, the size of the sintered RuCo@NC is further reduced, and its surface becomes rough. In addition, the TEM images of 1-RuCo- T_2 @NC750 obtained at different sintering temperatures are shown in Figure S1e–g. With the increase in sintering temperature, the agglomeration of RuCo nanoparticles becomes more and more serious. The detailed distribution of elements in catalyst was obtained by a high angle annular dark field scanning transmission electron microscope (HAADF-STEM). According to the results of the EDX elemental mapping displayed in Figure 2c, it can be clearly observed that Ru and Co elements in 1-RuCo500@NC750 are evenly distributed in the carbon matrix. Moreover, the contents of Ru and Co in each sample were determined by inductively coupled plasma mass spectrometry (ICP-MS) (Table S2).

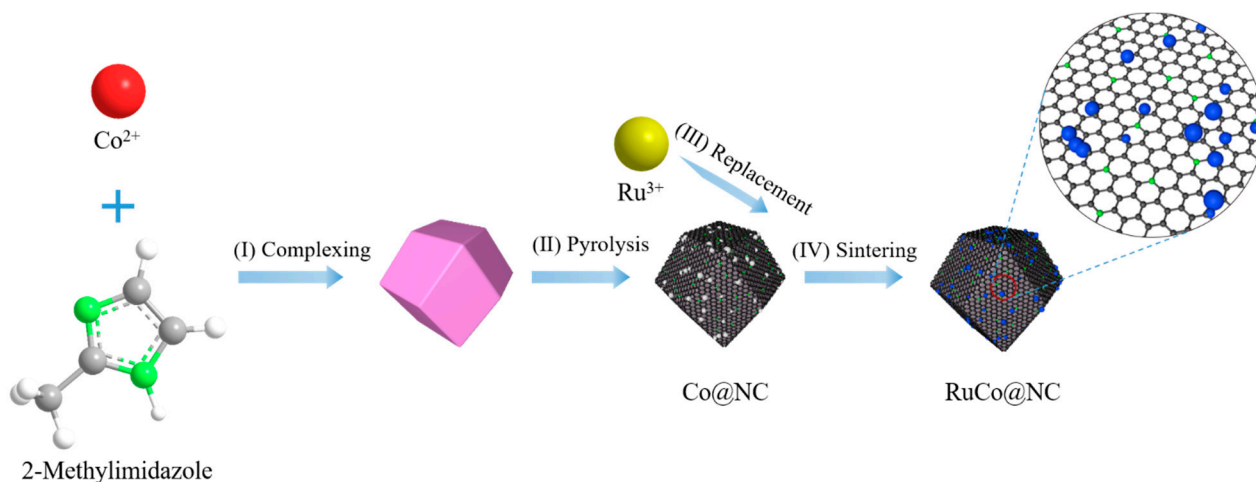


Figure 1. Schematic illustration of synthesis of RuCo@NC by a pyrolysis-displacement-sintering strategy.

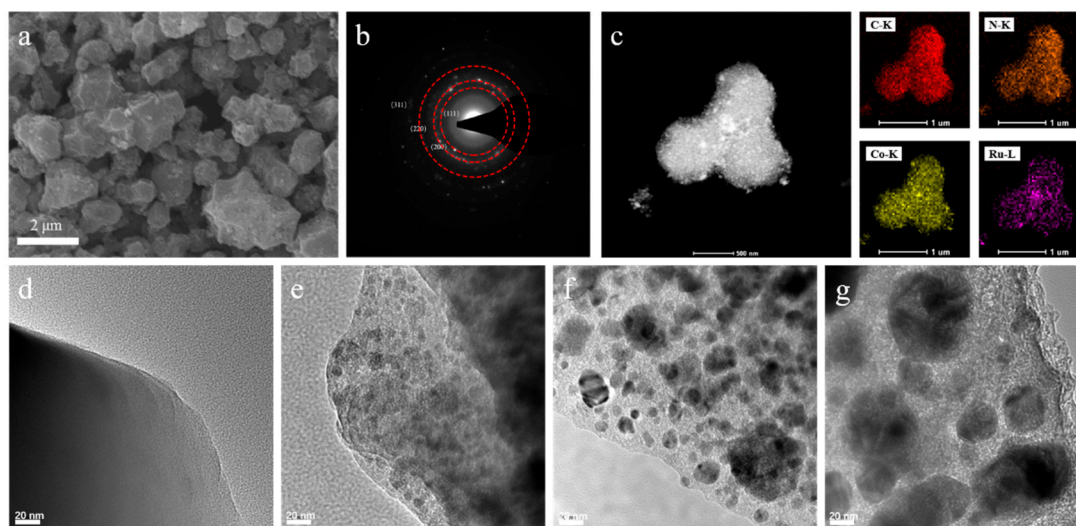


Figure 2. (a) SEM image of 1-RuCo500@NC750. (b) SAED pattern of $C_{ZIF67-750}$. (c) HAADF-STEM image and the corresponding elemental mapping images of 1-RuCo500@NC750. TEM images of (d) ZIF67, (e) $C_{ZIF67-600}$, (f) $C_{ZIF67-750}$, (g) $C_{ZIF67-900}$.

Powder X-ray diffraction (XRD) was conducted to further characterize the crystal phases and structures of $C_{ZIF67-T_1}$ (Figure 3a) and 1-RuCo- T_2 @NC750 (Figure 3b). The XRD pattern (Figure 3a) of ZIF67 is in agreement with those previously reported [34], proving that it has been successfully synthesized. In Figure 3a, the diffraction peaks at 75.8° , 51.5° and 44.2° of Co@NC-600 can be assigned to the (220), (200) and (111) faces of the face-centered cubic phase of metallic cobalt (PDF#15-0806), respectively, suggesting the presence of cobalt metal, which is in keeping with the results of SAED. Furthermore, with

the increase in pyrolysis temperature, the diffraction peaks of FCC-Co become stronger, indicating that the Co particles are larger, which is consistent with the results of TEM. Besides, the diffraction peak of graphite (002) plane appears when the sintering temperature is greater than 750 °C. As shown in Figure 3b, after the addition of Ru, the crystalline phase of RuCo@NC is found to be related to the annealing temperature. At low temperatures (e.g., 300 °C), the XRD patterns show only face-centered cubic phase cobalt metal (PDF#15-0806). However, the alloy phase of RuCo (PDF#65-8976) appears in addition to metallic cobalt at high temperatures (e.g., 500 and 700 °C), suggesting the coexistence of Co and RuCo metal particles in RuCo500@NC750 and RuCo700@NC750. For Ru NPs/C_{ZIF67}-750, XRD analysis was also carried out. Figure S5a shows that the hexagonal metallic Ru appears in the XRD pattern of Ru NPs/C_{ZIF67}-750 (PDF#89-3942), which indicates that Ru nanoparticles are successfully loaded on C_{ZIF67}-750.

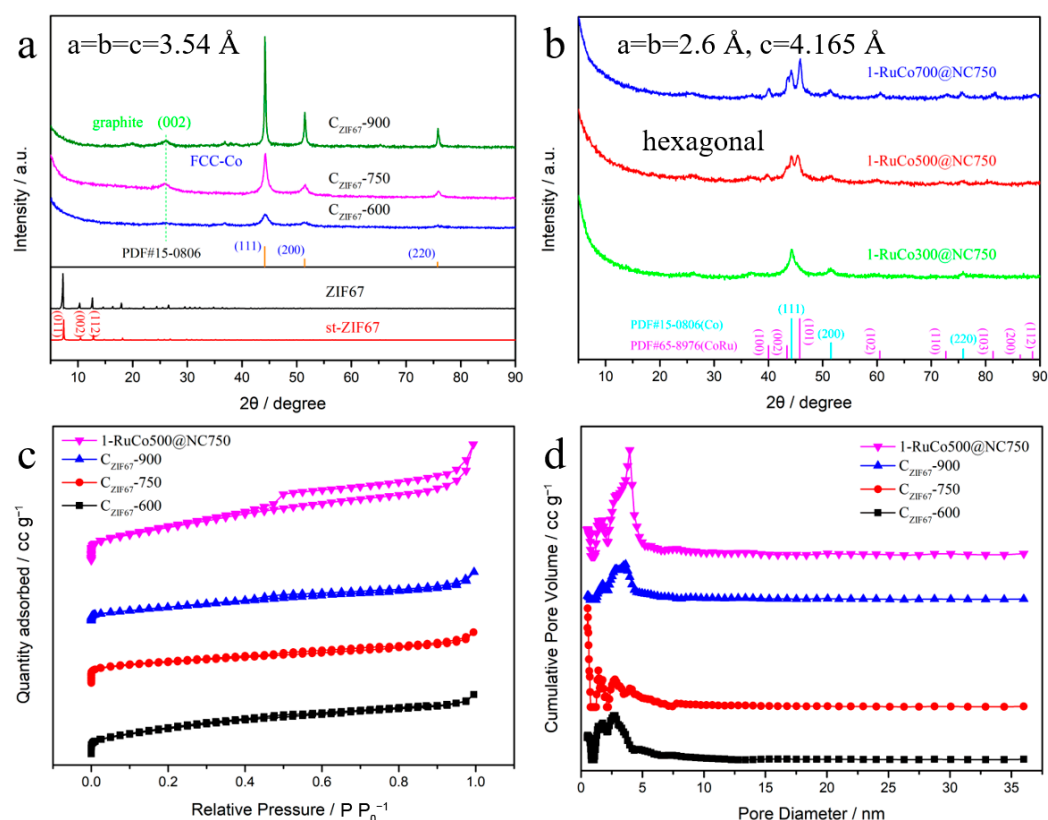


Figure 3. (a) X-ray diffraction patterns of ZIF67 and C_{ZIF67}-T₁ with different pyrolysis temperatures. (b) XRD patterns of 1-RuCo-T₂@NC750 with different sintering temperatures. (c) N₂ adsorption-desorption isotherms and (d) pore size distribution plots of C_{ZIF67}-T₁ with different pyrolysis temperatures and 1-RuCo500@NC750.

To further understand the porosity of materials, the specific surface area and pore size distribution of the samples were obtained by nitrogen (N₂) adsorption–desorption measurements. As shown in Figure 3c, the N₂ adsorption isotherms of 1-RuCo500@NC750 and C_{ZIF67}-T₁ belong to a type-IV isotherm with obvious type-H4 hysteresis loops. The rapid intake at relatively low pressures and hysteresis loops with P/P₀ values between 0.4 and 1.0 indicate that micropores and mesopores coexist in the samples, which is in accordance with the information of pore size distribution in Figure 3d. BET (Brunauer–Emmett–Teller) specific surface areas and pore volumes for C_{ZIF67}-T₁ and 1-RuCo500@NC750 are listed in Table S3. C_{ZIF67}-600 presents the minimum BET surface area of 57.21 m² g⁻¹, which may be due to the low pyrolysis temperature resulting in too few metal particles. When the pyrolysis temperature reaches 750 °C, the BET surface area increases sharply to 330.11 m² g⁻¹, which may be owing to the generation of more nanoparticles and graphitization of the

carbon matrix [41]. Meanwhile, the formation of nanoparticles also leads to a reduction in pore volume because they clog the pores. Nevertheless, the BET surface area of $C_{ZIF67-900}$ decreases to some extent, which may be caused by the agglomeration of nanoparticles. The BET surface area and pore volume of $1-RuCo500@NC750$ are much larger than that of $C_{ZIF67-750}$, which may be attributed to the fact that sintering results in more holes and a rough surface (Figure 2a). Higher BET specific surface area and larger pore volume are conducive to exposing more active sites, facilitating mass transfer and thus promoting HER performance [42].

In order to study the chemical valence states of each component element on the surface of the sample, X-ray photoelectron spectroscopy measurement was carried out. In the XPS spectra, Ru, Co, O, N and C elements can be observed on the surface of the sample. The N element arises from the ZIF67 precursor, while the O element comes from the oxidation of the catalyst by oxygen in air. As displayed in Figure 4b, the high-resolution N 1s spectrum of $C_{ZIF67-750}$ is fitted into two individual peaks at 397.8 and 399.5 eV, which are assigned to pyridinic-N and pyrrolic-N, respectively. Both types of N also exist in $1-RuCo500@NC750$. The successful addition of N atoms into the catalyst is able to regulate the local electronic structure of the carbon layer and raise the electrical conductivity of the carbon layer, which is beneficial to the improvement of the electrocatalytic performance [43]. The high-resolution Co 2p spectrum (Figure 4c) shows double prominent peaks located at 777.5 eV and 792.6 eV, proving the formation of metallic cobalt atoms in $C_{ZIF67-750}$. The peaks at 795.5 eV and 780.0 eV can be attributed to $Co^{2+} 2p_{1/2}$ and $Co^{2+} 2p_{3/2}$, respectively, as a result of the partial oxidation of the sample exposed to air. It is noteworthy that bivalent cobalt can effectively promote the water dissociation in the alkaline hydrogen evolution process [44]. Compared with $C_{ZIF67-750}$, the Co 2p XPS peaks of $1-RuCo500@NC750$ shift to a higher binding energy, probably as a result of a transfer of charge from Co, which is less electronegative, to Ru, which is more electronegative [3,31]. Only the peaks of Ru^0 are observed in the high resolution Ru 3p XPS spectra (Figure 4d) of the sample, revealing that all Ru^{3+} is reduced to elemental Ru during sintering [45]. In addition, with the increase in sintering temperature, the binding energies of Co 2p and Ru 3p shift to positive and negative directions (Figure 4d and Figure S2b) respectively, suggesting that a high temperature is favorable for electron transfer from Co to Ru. The effective electron transfer from Co to Ru in RuCo alloy nanoparticles can form appropriate metal-hydrogen binding energy, thereby improving the catalytic performance [45,46]. Additionally, XPS was used to determine the content of Ru and Co in $1-RuCo500@NC750$, as shown in Table S2. The cobalt content on the surface of the sample is significantly lower than the overall cobalt content because the cobalt on the surface is used to replace ruthenium in the solution.

3.2. Electrocatalytic Performances

The electrocatalytic HER performance of a sequence of samples in acidic (0.5 M H_2SO_4) and alkaline (1.0 M KOH) media was evaluated using a traditional three-electrode system. For comparison, Ru NPs/ $C_{ZIF67-750}$ and commercial Pt/C (JM, 20 wt.%) were also tested under equal conditions. Firstly, we studied the HER activities of $1-RuCo500@NC-T_1$ in alkaline conditions. As displayed in Figure 5a, the linear sweep voltammetry (LSV) curves of $1-RuCo500@NC750$ shows the minimum onset potential and maximum current density among the three samples generated at different pyrolysis temperatures, suggesting that 750 °C is the optimal pyrolysis temperature for $1-RuCo500@NC-T_1$. The reason may be that there are fewer cobalt nanoparticles produced at 600 °C which are difficult to displace Ru and form alloys, while the agglomeration of cobalt nanoparticles at 900 °C leads to the reduction in active sites. The same conclusion can be drawn from Figure S3a. Secondly, the HER activities of $1-RuCo-T_2@NC750$ were tested under alkaline conditions. As shown in Figure 5b, $1-RuCo500@NC750$ has better HER activity than the other two samples. Compared with the pyrolysis temperature, the sintering temperature has less influence on HER activity. Figure 5c shows that the overpotential of $3-RuCo500@NC750$ is very small, only 31 mV at 10 $mA\ cm^{-2}$, far lower than the 203.6 mV of Ru NPs/ $C_{ZIF67-750}$ and even the benchmark Pt/C (32.7 mV). At high overpotential, the advantage of

3-RuCo500@NC750 is more obvious (Figure 5d and Figure S3b), indicating that it has good alkaline HER catalytic activity. The Tafel slopes obtained from the polarization curve were utilized to study the intrinsic HER dynamics of catalysts. As shown in Figure 5e, the Tafel slope (47 mV dec^{-1}) of 3-RuCo500@NC750 is lower than that of commercial Pt/C (48 mV dec^{-1}) and Ru NPs/ $\text{C}_{\text{ZIF67-750}}$ (163 mV dec^{-1}), indicating that RuCo@NC-600 has the fastest kinetics for HER among them. Furthermore, the low Tafel slope value of 3-RuCo500@NC750 indicates that the HER takes place through the Volmer–Heyrovsky pathway [13]. In alkaline medium, the rate-determining step of both the material and Pt/C is the Volmer step. Because cobalt can accelerate the Volmer step, the material can achieve better performance than Pt/C. Electrochemical impedance spectroscopy (EIS) measurements can further disclose the kinetic characteristics of the catalyst (Figure S3d). The charge transfer resistance (R_{ct}) of 3-RuCo500@NC750 is 8.85Ω , which is much smaller than 24.97Ω of $\text{C}_{\text{ZIF67-750}}$ and 23.04Ω of Ru NPs/ $\text{C}_{\text{ZIF67-750}}$, implying that the interfacial charge transfer rate is faster after Ru doping. 3-RuCo500@NC750 has such excellent HER activity that it surpasses many of the most advanced catalysts reported to date (Table S4). Besides, the HER behavior was evaluated by calculating electrochemical surface area (ECSA), which is an important factor in determining overall catalytic activity. Because the electrochemical double-layer capacitance (C_{dl}) is linearly proportional to the electrochemical surface area of the catalyst, ECSA was obtained by measuring C_{dl} using cyclic voltammetry (CV) at different scanning rates ($0.01\text{--}0.1 \text{ V s}^{-1}$) (Figure S4). As displayed in Figure S3c, the C_{dl} value of 3-RuCo500@NC750 is as high as 63.81 mF cm^{-2} , which is the largest among all tested materials. Additionally, it is more than twice that of $\text{C}_{\text{ZIF67-750}}$ (30.15 mF cm^{-2}), indicating that the formation of RuCo alloy in the catalyst can offer more active sites to effectively improve HER activity. Durability reflects the long-term stability of the catalyst and is another important index to measure the practical value of electrocatalyst. Firstly, it is evaluated by potential-cycle accelerated durability test (ADT). As displayed in Figure 5f, 3-RuCo500@NC750 exhibits almost the same polarization curve after 1500 cycles, indicating good durability. Secondly, only a small increase in overpotential is observed in the 15 h chronopotentiometry test (Figure S6a), which further proves that it has robust stability in long-term operation. After the accelerated aging test, the crystal phase of 3-RuCo500@NC750 did not change significantly (Figure S5b), demonstrating that it has good structural stability in alkaline medium.

With the development of proton exchange membrane (PEM) electrolysis of water technology, acidic HER has received more and more attention [47,48]. As a consequence, the electrocatalytic HER performance of *n*-RuCo500@NC750 was also investigated under acidic conditions. In $0.5 \text{ M H}_2\text{SO}_4$ solution, 3-RuCo500@NC750 requires an overpotential of only 22 mV to obtain the current density of -10 mA cm^{-2} , much lower than that of Ru NPs/ $\text{C}_{\text{ZIF67-750}}$ (93.2 mV) and slightly higher than that of the reference Pt/C catalyst (15.6 mV). The same is true at high current densities, as shown in Figure 6b. Meanwhile, the Tafel slope of 3-RuCo500@NC750 in $0.5 \text{ M H}_2\text{SO}_4$ solution is 52 mV dec^{-1} , which is between the reference Pt/C (30 mV Dec^{-1}) and Ru NPs/ $\text{C}_{\text{ZIF67-750}}$ (90 mV Dec^{-1}), corresponding to a Volmer–Heyrovsky pathway. The low overpotential and Tafel slope indicate that 3-RuCo500@NC750 is an excellent acid electrocatalyst for hydrogen evolution, which exceeds many non-platinum electrocatalysts (Table S5). Although its hydrogen evolution activity is not as good as that of commercial 20 wt.% Pt/C, its cost is lower, so it still has some practical value for acidic HER. Likewise, we also obtain the electrochemical double-layer capacitance by cyclic voltammetry at different scan rates. The C_{dl} value of 3-RuCo500@NC750 is the largest among the tested samples (Figure 6d), indicating that it has the largest ECSA. From the point of view of the electrochemical impedance spectrum (Figure 6e), 3-RuCo500@NC750 has the smallest charge transfer resistance (4.34Ω), which is beneficial to reduce the energy consumption in the process of hydrogen evolution. In addition, the 3-RuCo500@NC750 also possesses the prominent cycling and long-term stabilities in acidic media, as assessed by chronopotentiometric measurements and the electrochemical accelerated durability tests (Figure 6f). After 3000 scanning cycles, the per-

formance degradation of 3-RuCo500@NC750 is almost negligible. In chronopotentiometry (Figure S6b), 3-RuCo500@NC750 maintained high HER activity for up to 15 h. Comparing the XRD patterns of the catalysts before and after the accelerated aging experiment, it is found that the crystal phase structure of the catalysts has little change, indicating that the catalyst has good stability and can run for a long time under acidic conditions.

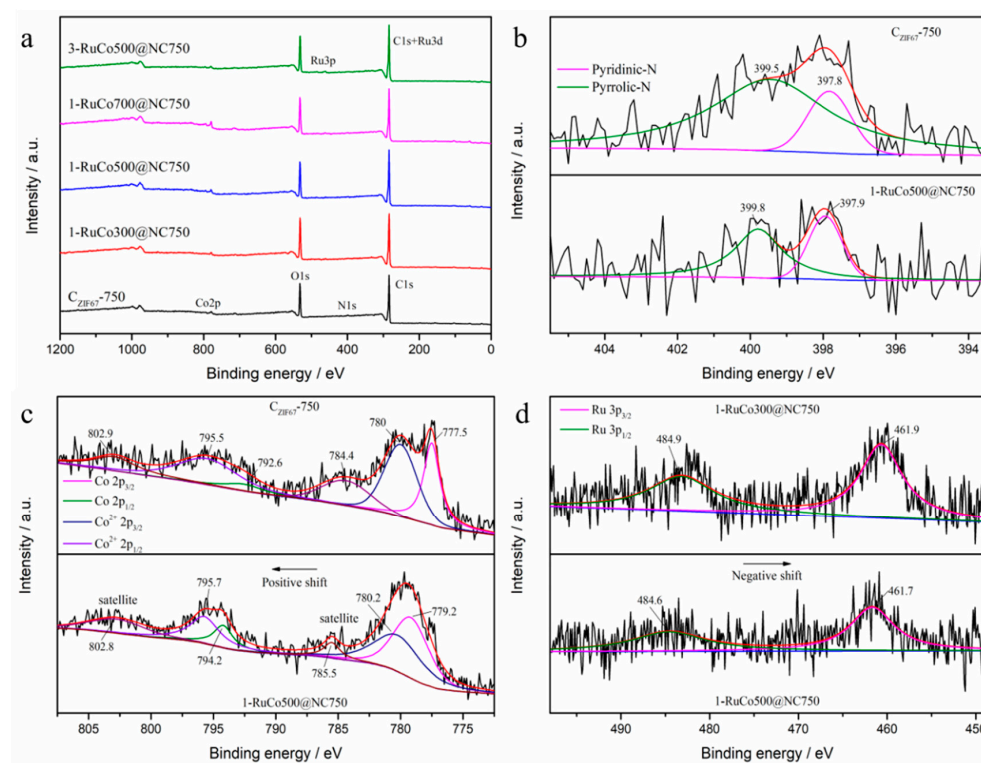


Figure 4. (a) XPS full spectra of RuCo- T_2 @NC750 and $C_{ZIF67-T1}$. High-resolution (b) N 1s and (c) Co 2p XPS spectra of $C_{ZIF67-750}$ and 1-RuCo500@NC750. (d) Ru 3p XPS spectra of 1-RuCo300@NC750 and 1-RuCo500@NC750.

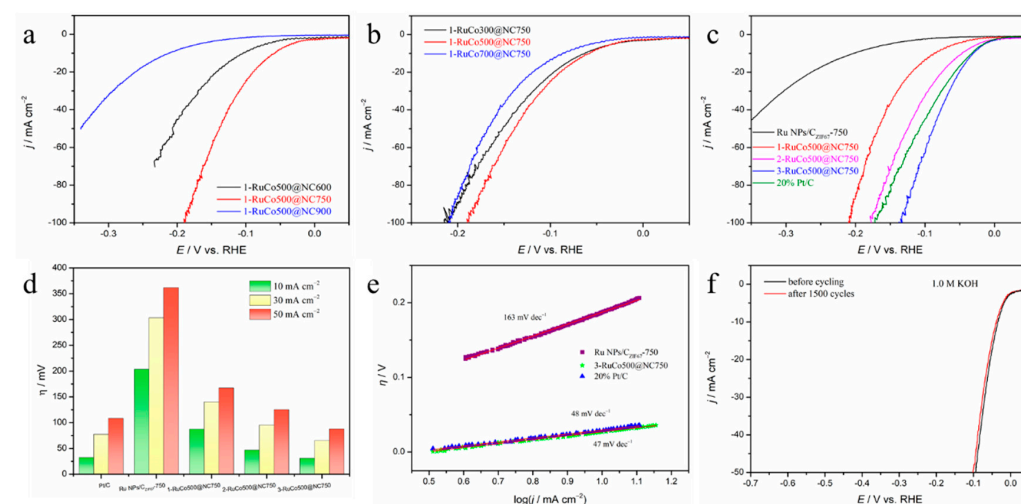


Figure 5. HER polarization curves of (a) 1-RuCo500@NC- T_1 and (b) 1-RuCo- T_2 @NC750 in 1.0 M KOH. (c) Comparison of HER activities of Ru NPs/ $C_{ZIF67-750}$, 20% Pt/C and n -RuCo500@NC750. (d) HER overpotential of Ru NPs/ $C_{ZIF67-750}$, 20% Pt/C and n -RuCo500@NC750 at different current densities (10, 30, 50 mA cm^{-2}). (e) Tafel plots of 3-RuCo500@NC750, Ru NPs/ $C_{ZIF67-750}$ and 20% Pt/C catalysts. (f) Polarization curves of 3-RuCo500@NC750 initially and after 1500 cycles during the accelerated durability tests.

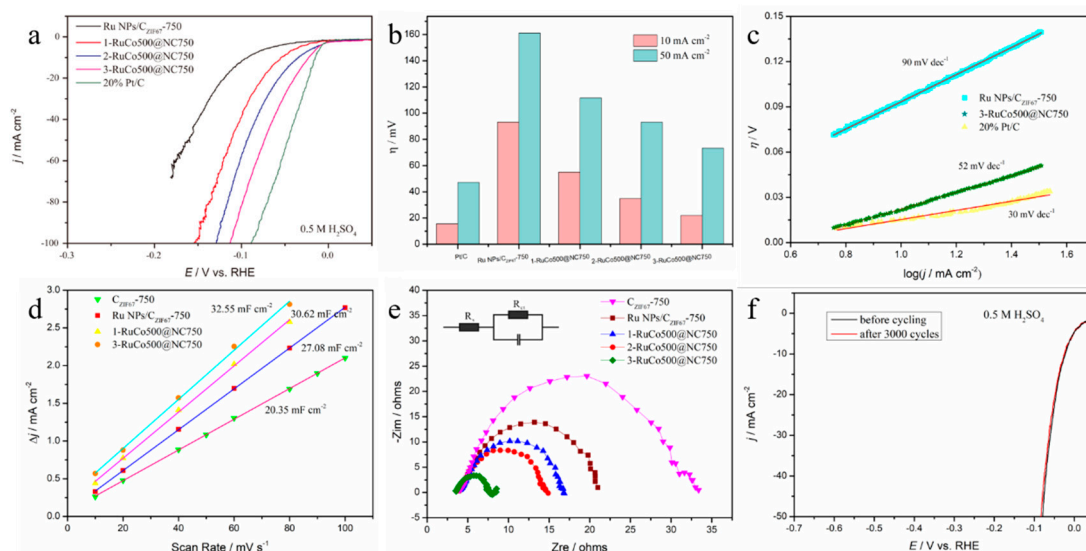


Figure 6. (a) HER polarization curves of Ru NPs/C_{ZIF67}-750, *n*-RuCo500@NC750 and 20% Pt/C in 0.5 M H₂SO₄. (b) HER overpotential of Ru NPs/C_{ZIF67}-750, 20% Pt/C and *n*-RuCo500@NC750 at different current densities (10, 30, 50 mA cm⁻²). (c) Tafel plots of 3-RuCo500@NC750, Ru NPs/C_{ZIF67}-750 and 20% Pt/C. (d) Linear fitting of capacitance current to CV scan rate for Ru NPs/C_{ZIF67}-750, *n*-RuCo500@NC750 and C_{ZIF67}-750. (e) Nyquist plots of Ru NPs/C_{ZIF67}-750, *n*-RuCo500@NC750 and C_{ZIF67}-750. (f) Polarization curves of 3-RuCo500@NC750 initially and after 3000 cycles during the accelerated durability tests.

Based on the foregoing results and discussion, the excellent electrocatalytic HER performance of 3-RuCo500@NC750 may be attributed to its unique composite structure and composition, mainly including the following: (1) The large electrochemical surface area provides more active sites for catalysis and the three-dimensional porous structure is beneficial for mass transport [49,50]. (2) Nitrogen-doped graphitized carbon matrix can improve the conductivity of the catalyst, which is conducive to the rapid transfer of electrons [43]. At the same time, the carbon matrix can protect the alloy nanoparticles from corrosion and prevent them from agglomeration [51]. (3) Alloy effect. According to the d-band center theory, the d-band center (E_d) energy level determines the adsorption intensity between the active site on the catalyst surface and the adsorption molecule [52,53]. The higher the energy level is, the stronger the adsorption capacity is [54]. Due to the high E_d energy level of single metal Ru, its adsorption capacity with H is strong, so its activity is poor when used as HER catalyst [55]. Co atoms, which are less electronegative, contribute electrons to Ru atoms when they form alloys. The electrons preferentially enter the bonding orbital of Ru, which reduces the E_d energy level of Ru, thus decreasing the strength of the Ru-H bond [52,54,56]. In summary, the 3-RuCo500@NC750 catalyst has outstanding catalytic performance due to the advantages of the structure and composition mentioned above.

4. Conclusions

In conclusion, we developed a simple pyrolysis-displacement-sintering strategy to manufacture RuCo alloy nanoparticles embedded in N-doped carbon as an excellent acid-base dual-use HER electrocatalyst. We found that RuCo alloy formed at a suitable pyrolysis temperature (500 °C) is more conducive to enhancing HER activity. The hydrogen evolution activity of the 3-RuCo500@NC750 with only 12.83 wt.% ruthenium content is better than that of commercial 20 wt.% Pt/C under alkaline conditions, and also outperforms that of most reported non-platinum catalysts under acidic conditions. Meanwhile, it also has a powerful stability and durability in both acid and alkaline media. The alloying of Ru and Co can adjust the d-band center energy level, so as to obtain high activity. Furthermore, cobalt can promote the decomposition of water, which is particularly important in basic hydrogen

evolution. Meanwhile, the presence of nitrogen-doped carbon matrix greatly enhances the stability of the catalyst. Combined with the experimental analysis, we believe that the superior HER performance of 3-RuCo500@NC750 is mainly attributed to its particular composite and composition, including its alloy effect, nanoscale effect, plentiful porous structure and conductive nitrogen-doped carbon matrix.

Supplementary Materials: The following supporting information can be downloaded at: <https://www.mdpi.com/article/10.3390/en15082908/s1>, Figure S1: SEM images of (a) ZIF67, (b) C_{ZIF67-750} and (c) 1-RuCo500@NC750. TEM images of (d) ZIF67, (e) 1-RuCo300@NC750, (f) 1-RuCo500@NC750 and (g) 1-RuCo700@NC750; Figure S2: (a) C 1s XPS spectrum of C_{ZIF67-750}. (b) Co 2p XPS spectra of 1-RuCo300@NC750 and 1-RuCo700@NC750; Figure S3: (a) HER polarization curves of 1-RuCo700@NC-T₁ in 1.0 M KOH. (b) HER mass activity of Ru NPs/C_{ZIF67-750}, 20% Pt/C and *n*-RuCo500@NC750 at −0.1 V. (c) Linear fitting of capacitance current to CV scan rate for Ru NPs/C_{ZIF67-750}, 1/3-RuCo500@NC750 and C_{ZIF67-750}. (d) Nyquist plots of Ru NPs/C_{ZIF67-750}, C_{ZIF67-750} and *n*-RuCo500@NC750; Figure S4: Cyclic voltammetry curves of C_{ZIF67-750}, Ru NPs/C_{ZIF67-750} and 1/3-RuCo500@NC750 at different scan rates in 1.0 M KOH; Figure S5: XRD patterns of (a) Ru NPs/C_{ZIF67-750} and (b) the 1-RuCo500@NC750 before and after HER test; Figure S6: The chronopotential response of 3-RuCo500@NC750 at the constant cathodic current density of −10 mA cm^{−2} in (a) 1.0 M KOH and (b) 0.5 M H₂SO₄; Table S1: The amount of RuCl₃ added in synthesis; Table S2: The Ru and Co content determined by ICP-MS and XPS; Table S3: BET surface areas and pore volumes of samples; Table S4: Compared with the reported performance of alkaline HER electrocatalysts; Table S5: Compared with the reported performance of acidic HER electrocatalysts [57–72].

Author Contributions: Formal analysis, C.W.; Funding acquisition, W.X.; Investigation, C.W.; Methodology, C.L.; Project administration, J.G.; Resources, G.S.; Software, W.L.; Validation, Y.W.; Visualization, Z.S.; Writing—original draft, C.W.; Writing—review & editing, G.S. and C.L. All authors have read and agreed to the published version of the manuscript.

Funding: This research was funded by the Instrument Developing Project of the Chinese Academy of Sciences, the Strategic Priority Research Program of the Chinese Academy of Sciences, grant number No. XDA21090400 and the Natural Science Foundation of Jilin Province, grant number 20190201300JC.

Institutional Review Board Statement: Not applicable.

Informed Consent Statement: Not applicable.

Data Availability Statement: The data used to support the findings of this study are available within the article.

Acknowledgments: Wei Xing acknowledge Gusu Talent program for the financial support.

Conflicts of Interest: The authors declare no conflict of interest.

References

1. Wang, H.; Chen, Z.N.; Wu, D.; Cao, M.; Sun, F.; Zhang, H.; You, H.; Zhuang, W.; Cao, R. Significantly Enhanced Overall Water Splitting Performance by Partial Oxidation of Ir through Au Modification in Core-Shell Alloy Structure. *J. Am. Chem. Soc.* **2021**, *143*, 4639–4645. [[CrossRef](#)] [[PubMed](#)]
2. Jiang, X.; Jang, H.; Liu, S.; Li, Z.; Kim, M.G.; Li, C.; Qin, Q.; Liu, X.; Cho, J. The Heterostructure of Ru₂P/WO₃/NPC Synergistically Promotes H₂O Dissociation for Improved Hydrogen Evolution. *Angew. Chem. Int. Ed. Engl.* **2021**, *60*, 4110–4116. [[CrossRef](#)] [[PubMed](#)]
3. Zhang, F.; Zhu, Y.; Chen, Y.; Lu, Y.; Lin, Q.; Zhang, L.; Tao, S.; Zhang, X.; Wang, H. RuCo alloy bimodal nanoparticles embedded in N-doped carbon: A superior pH-universal electrocatalyst outperforms benchmark Pt for the hydrogen evolution reaction. *J. Mater. Chem. A* **2020**, *8*, 12810–12820. [[CrossRef](#)]
4. Sengodan, S.; Lan, R.; Humphreys, J.; Du, D.; Xu, W.; Wang, H.; Tao, S. Advances in reforming and partial oxidation of hydrocarbons for hydrogen production and fuel cell applications. *Renew. Sustain. Energy Rev.* **2018**, *82*, 761–780. [[CrossRef](#)]
5. Wu, Z.; Wang, J.; Xia, K.; Lei, W.; Liu, X.; Wang, D. MoS₂–MoP heterostructured nanosheets on polymer-derived carbon as an electrocatalyst for hydrogen evolution reaction. *J. Mater. Chem. A* **2018**, *6*, 616–622. [[CrossRef](#)]
6. Qiu, T.; Liang, Z.; Guo, W.; Gao, S.; Qu, C.; Tabassum, H.; Zhang, H.; Zhu, B.; Zou, R.; Shao-Horn, Y. Highly exposed ruthenium-based electrocatalysts from bimetallic metal-organic frameworks for overall water splitting. *Nano Energy* **2019**, *58*, 1–10. [[CrossRef](#)]

7. Ji, L.; Wang, J.; Zuo, S.; Chen, Z. In Situ Preparation of Pt Nanoparticles Supported on N-Doped Carbon as Highly Efficient Electrocatalysts for Hydrogen Production. *J. Phys. Chem. C* **2017**, *121*, 8923–8930. [[CrossRef](#)]
8. Chen, Z.; Gong, W.; Cong, S.; Wang, Z.; Song, G.; Pan, T.; Tang, X.; Chen, J.; Lu, W.; Zhao, Z. Eutectoid-structured WC/W₂C heterostructures: A new platform for long-term alkaline hydrogen evolution reaction at low overpotentials. *Nano Energy* **2020**, *68*, 104335. [[CrossRef](#)]
9. Wang, J.; Cui, W.; Liu, Q.; Xing, Z.; Asiri, A.M.; Sun, X. Recent Progress in Cobalt-Based Heterogeneous Catalysts for Electrochemical Water Splitting. *Adv. Mater.* **2016**, *28*, 215–230. [[CrossRef](#)]
10. Chang, J.; Lv, Q.; Li, G.; Ge, J.; Liu, C.; Xing, W. Core-shell structured Ni₁₂P₅/Ni₃(PO₄)₂ hollow spheres as difunctional and efficient electrocatalysts for overall water electrolysis. *Appl. Catal. B Environ.* **2017**, *204*, 486–496. [[CrossRef](#)]
11. Luo, Z.; Zhang, H.; Yang, Y.; Wang, X.; Li, Y.; Jin, Z.; Jiang, Z.; Liu, C.; Xing, W.; Ge, J. Reactant friendly hydrogen evolution interface based on di-anionic MoS₂ surface. *Nat. Commun.* **2020**, *11*, 1116. [[CrossRef](#)] [[PubMed](#)]
12. Samy, O.; El Moutaouakil, A. A Review on MoS₂ Energy Applications: Recent Developments and Challenges. *Energies* **2021**, *14*, 4586. [[CrossRef](#)]
13. Zhu, J.; Hu, L.; Zhao, P.; Lee, L.Y.S.; Wong, K.Y. Recent Advances in Electrocatalytic Hydrogen Evolution Using Nanoparticles. *Chem. Rev.* **2020**, *120*, 851–918. [[CrossRef](#)] [[PubMed](#)]
14. Shi, Y.; Dai, W.; Wang, M.; Xing, Y.; Xia, X.; Chen, W. Bioinspired Construction of Ruthenium-decorated Nitrogen-doped Graphene Aerogel as an Efficient Electrocatalyst for Hydrogen Evolution Reaction. *Chem. Res. Chin. Univ.* **2020**, *36*, 709–714. [[CrossRef](#)]
15. Mitchell, W.J.; Xie, J.; Jachimowski, T.A.; Weinberg, W.H. Carbon monoxide hydrogenation on the Ru (001) surface at low temperature using gas-phase atomic hydrogen: Spectroscopic evidence for the carbonyl insertion mechanism on a transition metal surface. *J. Am. Chem. Soc.* **1995**, *117*, 2606–2617. [[CrossRef](#)]
16. Alberas, D.J.; Kiss, J.; Liu, Z.M.; White, J.M. Surface chemistry of hydrazine on Pt(111). *Surf. Sci.* **1992**, *278*, 51–61. [[CrossRef](#)]
17. Zheng, Y.; Jiao, Y.; Zhu, Y.; Li, L.H.; Han, Y.; Chen, Y.; Jaroniec, M.; Qiao, S.-Z. High electrocatalytic hydrogen evolution activity of an anomalous ruthenium catalyst. *J. Am. Chem. Soc.* **2016**, *138*, 16174–16181. [[CrossRef](#)]
18. Mahmood, J.; Li, F.; Jung, S.-M.; Okyay, M.S.; Ahmad, I.; Kim, S.-J.; Park, N.; Jeong, H.Y.; Baek, J.-B. An efficient and pH-universal ruthenium-based catalyst for the hydrogen evolution reaction. *Nat. Nanotechnol.* **2017**, *12*, 441–446. [[CrossRef](#)]
19. Wang, W.; Yuan, T.; Tang, H.; Hu, Z.; Wang, Y.; Liu, Q. Ruthenium nanoparticles supported on carbon oxide nanotubes for electrocatalytic hydrogen evolution in alkaline media. *Chem. Phys. Lett.* **2021**, *779*, 138879. [[CrossRef](#)]
20. Xie, L.; Ren, X.; Liu, Q.; Cui, G.; Ge, R.; Asiri, A.M.; Sun, X.; Zhang, Q.; Chen, L. A Ni(OH)₂-PtO₂ hybrid nanosheet array with ultralow Pt loading toward efficient and durable alkaline hydrogen evolution. *J. Mater. Chem. A* **2018**, *6*, 1967–1970. [[CrossRef](#)]
21. Cao, X.; Han, Y.; Gao, C.; Xu, Y.; Huang, X.; Willander, M.; Wang, N. Highly catalytic active PtNiCu nanochains for hydrogen evolution reaction. *Nano Energy* **2014**, *9*, 301–308. [[CrossRef](#)]
22. Sarabia, F.J.; Sebastian-Pascual, P.; Koper, M.T.M.; Climent, V.; Feliu, J.M. Effect of the Interfacial Water Structure on the Hydrogen Evolution Reaction on Pt(111) Modified with Different Nickel Hydroxide Coverages in Alkaline Media. *ACS Appl. Mater. Interfaces* **2019**, *11*, 613–623. [[CrossRef](#)] [[PubMed](#)]
23. Lu, X.F.; Yu, L.; Lou, X.W. Highly crystalline Ni-doped FeP/carbon hollow nanorods as all-pH efficient and durable hydrogen evolving electrocatalysts. *Sci. Adv.* **2019**, *5*, eaav6009. [[CrossRef](#)] [[PubMed](#)]
24. Angeles-Olvera, Z.; Crespo-Yapur, A.; Rodríguez, O.; Cholula-Díaz, J.L.; Martínez, L.M.; Videa, M. Nickel-Based Electrocatalysts for Water Electrolysis. *Energies* **2022**, *15*, 1609. [[CrossRef](#)]
25. Kyriakou, G.; Boucher, M.B.; Jewell, A.D.; Lewis, E.A.; Lawton, T.J.; Baber, A.E.; Tierney, H.L.; Flytzani-Stephanopoulos, M.; Sykes, E.C.H. Isolated Metal Atom Geometries as a Strategy for Selective Heterogeneous Hydrogenations. *Science* **2012**, *335*, 1209–1212. [[CrossRef](#)]
26. Feng, X.; Wang, H.; Bo, X.; Guo, L. Bimetal-organic framework-derived porous rodlike Cobalt/Nickel nitride for All-pH value electrochemical hydrogen evolution. *ACS Appl. Mater. Interfaces* **2019**, *11*, 8018–8024. [[CrossRef](#)]
27. Tu, K.; Tranca, D.; Rodriguez-Hernandez, F.; Jiang, K.; Huang, S.; Zheng, Q.; Chen, M.X.; Lu, C.; Su, Y.; Chen, Z.; et al. A Novel Heterostructure Based on RuMo Nanoalloys and N-doped Carbon as an Efficient Electrocatalyst for the Hydrogen Evolution Reaction. *Adv. Mater.* **2020**, *32*, e2005433. [[CrossRef](#)]
28. Darling, A.J.; Stewart, S.; Holder, C.F.; Schaak, R.E. Bulk-immiscible AgRh Alloy Nanoparticles as a Highly Active Electrocatalyst for the Hydrogen Evolution Reaction. *ChemNanoMat* **2020**, *6*, 1320–1324. [[CrossRef](#)]
29. Dong, J.; Sun, T.; Zhang, Y.; Zhang, H.; Lu, S.; Hu, D.; Chen, J.; Xu, L. Mesoporous NiCo alloy/reduced graphene oxide nanocomposites as efficient hydrogen evolution catalysts. *J. Colloid Interface Sci.* **2021**, *599*, 603–610. [[CrossRef](#)]
30. Chen, H.; Yuan, M.; Zhai, C.; Tan, L.; Cong, N.; Han, J.; Fang, H.; Zhou, X.; Ren, Z.; Zhu, Y. Nano PdFe Alloy Assembled Film as a Highly Efficient Electrocatalyst toward Hydrogen Evolution in Both Acid and Alkaline Solutions. *ACS Appl. Energy Mater.* **2020**, *3*, 8969–8977. [[CrossRef](#)]
31. Wu, Q.; Luo, M.; Han, J.; Peng, W.; Zhao, Y.; Chen, D.; Peng, M.; Liu, J.; de Groot, F.M.F.; Tan, Y. Identifying Electrocatalytic Sites of the Nanoporous Copper-Ruthenium Alloy for Hydrogen Evolution Reaction in Alkaline Electrolyte. *ACS Energy Lett.* **2019**, *5*, 192–199. [[CrossRef](#)]
32. Chen, J.; Xia, G.; Jiang, P.; Yang, Y.; Li, R.; Shi, R.; Su, J.; Chen, Q. Active and Durable Hydrogen Evolution Reaction Catalyst Derived from Pd-Doped Metal-Organic Frameworks. *ACS Appl. Mater. Interfaces* **2016**, *8*, 13378–13383. [[CrossRef](#)] [[PubMed](#)]

33. Li, B.; Ma, J.G.; Cheng, P. Integration of metal nanoparticles into metal–organic frameworks for composite catalysts: Design and synthetic strategy. *Small* **2019**, *15*, 1804849. [[CrossRef](#)] [[PubMed](#)]
34. Liang, L.; Jin, H.; Zhou, H.; Liu, B.; Hu, C.; Chen, D.; Wang, Z.; Hu, Z.; Zhao, Y.; Li, H.-W.; et al. Cobalt single atom site isolated Pt nanoparticles for efficient ORR and HER in acid media. *Nano Energy* **2021**, *88*, 106221. [[CrossRef](#)]
35. Yang, Q.; Xu, Q.; Yu, S.H.; Jiang, H.L. Pd Nanocubes@ZIF-8: Integration of Plasmon-Driven Photothermal Conversion with a Metal-Organic Framework for Efficient and Selective Catalysis. *Angew. Chem. Int. Ed. Engl.* **2016**, *55*, 3685–3689. [[CrossRef](#)]
36. Li, X.; Zhao, S.; Zhang, W.; Liu, Y.; Li, R. Ru nanoparticles supported on nitrogen-doped porous carbon derived from ZIF-8 as an efficient catalyst for the selective hydrogenation of p-chloronitrobenzene and p-bromonitrobenzene. *Dalton Trans.* **2016**, *45*, 15595–15602. [[CrossRef](#)]
37. Wu, Y.L.; Li, X.; Wei, Y.S.; Fu, Z.; Wei, W.; Wu, X.T.; Zhu, Q.L.; Xu, Q. Ordered Macroporous Superstructure of Nitrogen-Doped Nanoporous Carbon Implanted with Ultrafine Ru Nanoclusters for Efficient pH-Universal Hydrogen Evolution Reaction. *Adv. Mater.* **2021**, *33*, e2006965. [[CrossRef](#)]
38. Yun, R.; Zhan, F.; Wang, X.; Zhang, B.; Sheng, T.; Xin, Z.; Mao, J.; Liu, S.; Zheng, B. Design of Binary Cu-Fe Sites Coordinated with Nitrogen Dispersed in the Porous Carbon for Synergistic CO₂ Electroreduction. *Small* **2021**, *17*, e2006951. [[CrossRef](#)]
39. Chen, C.-H.; Chiou, T.-W.; Chang, H.-C.; Li, W.-L.; Tung, C.-Y.; Liaw, W.-F. An organic ligand promoting the electrocatalytic activity of cobalt oxide for the hydrogen evolution reaction. *Sustain. Energy Fuels* **2019**, *3*, 2205–2210. [[CrossRef](#)]
40. Wang, Z.; Ke, X.; Zhou, K.; Xu, X.; Jin, Y.; Wang, H.; Sui, M. Engineering the structure of ZIF-derived catalysts by revealing the critical role of temperature for enhanced oxygen reduction reaction. *J. Mater. Chem. A* **2021**, *9*, 18515–18525. [[CrossRef](#)]
41. Gong, Y.; Li, D.; Luo, C.; Fu, Q.; Pan, C. Highly porous graphitic biomass carbon as advanced electrode materials for supercapacitors. *Green Chem.* **2017**, *19*, 4132–4140. [[CrossRef](#)]
42. Ao, X.; Zhang, W.; Li, Z.; Li, J.-G.; Soule, L.; Huang, X.; Chiang, W.-H.; Chen, H.M.; Wang, C.; Liu, M. Markedly enhanced oxygen reduction activity of single-atom Fe catalysts via integration with Fe nanoclusters. *ACS Nano* **2019**, *13*, 11853–11862. [[CrossRef](#)] [[PubMed](#)]
43. Su, C.Y.; Cheng, H.; Li, W.; Liu, Z.Q.; Li, N.; Hou, Z.; Bai, F.Q.; Zhang, H.X.; Ma, T.Y. Atomic modulation of FeCo–nitrogen–carbon bifunctional oxygen electrodes for rechargeable and flexible all-solid-state zinc–air battery. *Adv. Energy Mater.* **2017**, *7*, 1602420. [[CrossRef](#)]
44. Wang, Z.; Ren, X.; Luo, Y.; Wang, L.; Cui, G.; Xie, F.; Wang, H.; Xie, Y.; Sun, X. An ultrafine platinum–cobalt alloy decorated cobalt nanowire array with superb activity toward alkaline hydrogen evolution. *Nanoscale* **2018**, *10*, 12302–12307. [[CrossRef](#)] [[PubMed](#)]
45. Li, M.; Wang, H.; Zhu, W.; Li, W.; Wang, C.; Lu, X. RuNi nanoparticles embedded in N-doped carbon nanofibers as a robust bifunctional catalyst for efficient overall water splitting. *Adv. Sci.* **2020**, *7*, 1901833. [[CrossRef](#)]
46. Yang, J.; Shao, Q.; Huang, B.; Sun, M.; Huang, X. pH-universal water splitting catalyst: Ru-Ni nanosheet assemblies. *Iscience* **2019**, *11*, 492–504. [[CrossRef](#)] [[PubMed](#)]
47. Shiva Kumar, S.; Ramakrishna, S.U.B.; Rama Devi, B.; Himabindu, V. Phosphorus-doped graphene supported palladium (Pd/Pg) electrocatalyst for the hydrogen evolution reaction in PEM water electrolysis. *Int. J. Green Energy* **2018**, *15*, 558–567. [[CrossRef](#)]
48. Brito, J.; Restivo, J.; Sousa, J.P.S.; Spera, N.C.M.; Falcão, D.S.; Rocha, A.; Pinto, A.M.F.R.; Pereira, M.F.R.; Soares, O.S.G.P. Implementation of Transition Metal Phosphides as Pt-Free Catalysts for PEM Water Electrolysis. *Energies* **2022**, *15*, 1821. [[CrossRef](#)]
49. Wang, J.; Zhu, H.; Yu, D.; Chen, J.; Chen, J.; Zhang, M.; Wang, L.; Du, M. Engineering the Composition and Structure of Bimetallic Au–Cu Alloy Nanoparticles in Carbon Nanofibers: Self-Supported Electrode Materials for Electrocatalytic Water Splitting. *ACS Appl. Mater. Interfaces* **2017**, *9*, 19756–19765. [[CrossRef](#)]
50. Zhong, X.; Jiang, Y.; Chen, X.; Wang, L.; Zhuang, G.; Li, X.; Wang, J.-G. Integrating cobalt phosphide and cobalt nitride-embedded nitrogen-rich nanocarbons: High-performance bifunctional electrocatalysts for oxygen reduction and evolution. *J. Mater. Chem. A* **2016**, *4*, 10575–10584. [[CrossRef](#)]
51. Xu, Y.; Yin, S.; Li, C.; Deng, K.; Xue, H.; Li, X.; Wang, H.; Wang, L. Low-ruthenium-content NiRu nanoalloys encapsulated in nitrogen-doped carbon as highly efficient and pH-universal electrocatalysts for the hydrogen evolution reaction. *J. Mater. Chem. A* **2018**, *6*, 1376–1381. [[CrossRef](#)]
52. Nørskov, J.K.; Bligaard, T.; Rossmeisl, J.; Christensen, C.H. Towards the computational design of solid catalysts. *Nat. Chem.* **2009**, *1*, 37–46. [[CrossRef](#)] [[PubMed](#)]
53. Hammer, B.; Nørskov, J.K. Electronic factors determining the reactivity of metal surfaces. *Surface Science* **1995**, *343*, 211–220. [[CrossRef](#)]
54. Sun, S.; Zhou, X.; Cong, B.; Hong, W.; Chen, G. Tailoring the d-Band Centers Endows (Ni_xFe_{1-x})₂P Nanosheets with Efficient Oxygen Evolution Catalysis. *ACS Catal.* **2020**, *10*, 9086–9097. [[CrossRef](#)]
55. Gou, W.; Li, J.; Gao, W.; Xia, Z.; Zhang, S.; Ma, Y. Downshifted d-Band Center of Ru/MWCNTs by Turbostratic Carbon Nitride for Efficient and Robust Hydrogen Evolution in Alkali. *ChemCatChem* **2019**, *11*, 1970–1976. [[CrossRef](#)]
56. Nørskov, J.K.; Abild-Pedersen, F.; Studt, F.; Bligaard, T. Density functional theory in surface chemistry and catalysis. *Proc. Natl. Acad. Sci. USA* **2011**, *108*, 937–943. [[CrossRef](#)]
57. Bhowmik, T.; Kundu, M.K.; Barman, S. Growth of One-Dimensional RuO₂ Nanowires on g-Carbon Nitride: An Active and Stable Bifunctional Electrocatalyst for Hydrogen and Oxygen Evolution Reactions at All pH Values. *ACS Appl. Mater. Interfaces* **2016**, *8*, 28678–28688. [[CrossRef](#)]

58. Wang, Z.; Wang, S.; Ma, L.; Guo, Y.; Sun, J.; Zhang, N.; Jiang, R. Water-Induced Formation of Ni₂P-Ni₁₂P₅ Interfaces with Superior Electrocatalytic Activity toward Hydrogen Evolution Reaction. *Small* **2021**, *17*, e2006770. [[CrossRef](#)]
59. Song, H.; Wu, M.; Tang, Z.; Tse, J.S.; Yang, B.; Lu, S. Single Atom Ruthenium-Doped CoP/CDs Nanosheets via Splicing of Carbon-Dots for Robust Hydrogen Production. *Angew. Chem. Int. Ed. Engl.* **2021**, *60*, 7234–7244. [[CrossRef](#)]
60. Lin, F.; Qin, H.; Wang, T.; Yang, L.; Cao, X.; Jiao, L. Few-layered MoN–MnO heterostructures with interfacial-O synergistic active centers boosting electrocatalytic hydrogen evolution. *J. Mater. Chem. A* **2021**, *9*, 8325–8331. [[CrossRef](#)]
61. Yang, Y.; Qian, Y.; Li, H.; Zhang, Z.; Mu, Y.; Do, D.; Zhou, B.; Dong, J.; Yan, W.; Qin, Y.; et al. O-coordinated W-Mo dual-atom catalyst for pH-universal electrocatalytic hydrogen evolution. *Sci. Adv.* **2020**, *6*, eaba6586. [[CrossRef](#)] [[PubMed](#)]
62. Wu, L.; Zhang, M.; Wen, Z.; Ci, S. V₈C₇ decorating CoP nanosheets-assembled microspheres as trifunctional catalysts toward energy-saving electrolytic hydrogen production. *Chem. Eng. J.* **2020**, *399*, 125728. [[CrossRef](#)]
63. Wang, J.; Zhang, Z.; Song, H.; Zhang, B.; Liu, J.; Shai, X.; Miao, L. Water Dissociation Kinetic-Oriented Design of Nickel Sulfides via Tailored Dual Sites for Efficient Alkaline Hydrogen Evolution. *Adv. Funct. Mater.* **2020**, *31*, 2008578. [[CrossRef](#)]
64. Jin, D.; Yu, A.; Lee, Y.; Kim, M.H.; Lee, C. Ni_xRh_{1-x} bimetallic alloy nanofibers as a pH-universal electrocatalyst for the hydrogen evolution reaction: The synthetic strategy and fascinating electroactivity. *J. Mater. Chem. A* **2020**, *8*, 8629–8637. [[CrossRef](#)]
65. Fan, J.; Wu, J.; Cui, X.; Gu, L.; Zhang, Q.; Meng, F.; Lei, B.H.; Singh, D.J.; Zheng, W. Hydrogen Stabilized RhPdH 2D Bimetallic Nanosheets for Efficient Alkaline Hydrogen Evolution. *J. Am. Chem. Soc.* **2020**, *142*, 3645–3651. [[CrossRef](#)]
66. Jebaslinhepybai, B.T.; Prabu, N.; Sasidharan, M. Facile galvanic replacement method for porous Pd@Pt nanoparticles as an efficient HER electrocatalyst. *Int. J. Hydrogen Energy* **2020**, *45*, 11127–11137. [[CrossRef](#)]
67. Dai, X.; Du, K.; Li, Z.; Liu, M.; Ma, Y.; Sun, H.; Zhang, X.; Yang, Y. Co-Doped MoS₂ Nanosheets with the Dominant CoMoS Phase Coated on Carbon as an Excellent Electrocatalyst for Hydrogen Evolution. *ACS Appl. Mater. Interfaces* **2015**, *7*, 27242–27253. [[CrossRef](#)]
68. Zhu, J.; Guo, Y.; Liu, F.; Xu, H.; Gong, L.; Shi, W.; Chen, D.; Wang, P.; Yang, Y.; Zhang, C.; et al. Regulative Electronic States around Ruthenium/Ruthenium Disulphide Heterointerfaces for Efficient Water Splitting in Acidic Media. *Angew. Chem. Int. Ed. Engl.* **2021**, *60*, 12328–12334. [[CrossRef](#)]
69. Zhao, C.; Yu, Z.; Xing, J.; Zou, Y.; Liu, H.; Zhang, H.; Yu, W.; Idriss, H.; Guo, C. Effect of Ag₂S Nanocrystals/Reduced Graphene Oxide Interface on Hydrogen Evolution Reaction. *Catalysts* **2020**, *10*, 948. [[CrossRef](#)]
70. Zhang, H.; Zhou, W.; Lu, X.F.; Chen, T.; Lou, X.W. Implanting Isolated Ru Atoms into Edge-Rich Carbon Matrix for Efficient Electrocatalytic Hydrogen Evolution. *Adv. Energy Mater.* **2020**, *10*, 2000882. [[CrossRef](#)]
71. Yu, X.-P.; Yang, C.; Song, P.; Peng, J. Self-assembly of Au/MoS₂ quantum dots core-satellite hybrid as efficient electrocatalyst for hydrogen production. *Tungsten* **2020**, *2*, 194–202. [[CrossRef](#)]
72. Yang, W.; Zhang, S.; Chen, Q.; Zhang, C.; Wei, Y.; Jiang, H.; Lin, Y.; Zhao, M.; He, Q.; Wang, X.; et al. Conversion of Intercalated MoO₃ to Multi-Heteroatoms-Doped MoS₂ with High Hydrogen Evolution Activity. *Adv. Mater.* **2020**, *32*, e2001167. [[CrossRef](#)] [[PubMed](#)]